P-doped $Zn_xCd_{1-x}S$ solid solutions as photocatalysts for hydrogen evolution from water splitting coupled with photocatalytic oxidation of 5-hydroxymethylfurfural

Hui-Fang Ye[a,b], Rui Shi[a], Xiao Yang[a,b], Wen-Fu Fu[a], Yong Chen[a,b,*]

[a] Key Laboratory of Photochemical Conversion and Optoelectronic Materials & HKU-CAS Joint Laboratory on New Materials, Technical Institute of Physics and Chemistry, Chinese Academy of Sciences, Beijing 100190, PR China
[b] University of Chinese Academy of Sciences, Beijing 100149, PR China

ARTICLE INFO

ABSTRACT

Photocatalytic water splitting over semiconductors without using of any electron sacrificial agents is essential to the conversion of solar energy into chemical energy. Herein, we report remarkable photocatalytic hydrogen production from pure water without the assistance of electron sacrificial agents by using P-doped $Zn_xCd_{1-x}S$ with rich S vacancies ($Zn_xCd_{1-x}S$-P) as the photocatalyst. It is found that interstitial P doping in $Zn_xCd_{1-x}S$ solid solutions with rich S vacancies can prolong the lifetime of charge carriers and enhance the generation and separation of photogenerated electrons-holes, resulting in a H_2 evolution rate of up to 419 μmol h^{-1} g^{-1}, which is 72 and 7.5 times higher than those of ZnS-P (5.8 μmol h^{-1} g^{-1}) and CdS-P (56 μmol h^{-1} g^{-1}), respectively. Furthermore, the introduction of biomass-derived compound 5-hydroxymethylfurfural (HMF) into this system further promotes the photocatalytic hydorgen evolution reaction and simultaneously obtains value-added HMF oxidation products.

1. Introduction

Solar-driven water splitting over semiconductor photocatalysts is a promising approach for converting solar energy into renewable and storable chemical energy. In the past decades, substantial efforts have been devoted to direct splitting of water into H_2 and O_2 under sunlight irradiation [1–6]. The general strategy for achieving overall water splitting is to simultaneously load oxidation and reduction co-catalysts on semiconductors possessing suitable conduction and valence band positions, which provide surface redox reaction sites that can catalyze oxygen and hydrogen evolution reactions with relatively low activation energies [7–10]. However, semiconductors that have suitable band structures and nice absorption in the visible region are rare. Inspired by natural photosynthesis in green plants, so-called Z-scheme photocatalytic systems have been developed by combining two different semiconductors which can function as H_2-evolving and O_2-evolving photocatalysts, respectively [11–14]. However, the efficiency of these overall water splitting systems is rather low and the development of novel semiconductor photocatalystic systems is still highly desirable.

Recently, we reported that phosphorus-doped CdS with rich S vacancies (CdS-P) can act as an efficient photocatalyst for photocatalytic

hydrogen evolution from pure water without using of any electron sacrificial agents under visible light irradiation [15]. It is found that the Fermi level of CdS is raised to approach the level of S vacancies after P doping, which makes the S vacancies become excellent electron trap centers. The appearance of electron trap centers is beneficial to prolong the lifetime of photogenerated electrons. Then, the long-lived photogenerated electrons are able to reach the surface active sites to initiate a photocatalytic hydrogen evolution reaction. This provides a new strategy for photocatalytic hydrogen evolution from pure water using a single semiconductor. Unfortunately, almost no O_2 was detected and only ·OH was observed through in situ EPR spectroscopy in this system, which can be attributed to the complex thermodynamics and sluggish reaction kinetics of photocatalytic oxygen evolution from water [16–19]. In consideration of the low economic value of O_2, one solution to promoting the efficiency of water splitting is to replace the oxygen evolution reaction by a more thermodynamics favorable and valuable photocatalytic oxidation reaction. In recent years, the conversion of renewable biomass resources into value-added chemicals for relieving the current energy crisis has attracted increasing attention. As one of the representative biomass-derived intermediates, 5-hydroxymethylfurfural requires further refining to become much higher

* Corresponding author at: Key Laboratory of Photochemical Conversion and Optoelectronic Materials & HKU-CAS Joint Laboratory on New Materials, Technical Institute of Physics and Chemistry, Chinese Academy of Sciences, Beijing 100190, PR China.
E-mail address: chenyong@mail.ipc.ac.cn (Y. Chen).

valued products. Sun et al. reported that electrocatalytic oxidation of HMF can be integrated with electrocatalytic hydrogen production in aqueous media [20–23]. Very recently, simultaneous photocatalytic hydrogen evolution and HMF oxidation was carried out using two-dimensional Ni/CdS nanosheets under visible light irradiation [24]. Compared with common electron sacrificial reagents such as lactic acid [25] and $Na_2S-Na_2SO_3$ solution [26], biomass-derived intermediate HMF can not only effectively utilize photogenerated holes and thus promote the separation of photogenerated charges, but also obtain value-added chemicals and improve the transformation of solar energy into storable chemicals under ambient conditions.

$Zn_xCd_{1-x}S$ solid solutions possess higher photocatalytic activities relative to pristine CdS and ZnS under visible light irradiation [27–36]. Through further modification via various strategies such as constructing heterogeneous structures [37–39], introducing co-catalysts [40,41], and metal doping [42], the resulting hybrid $Zn_xCd_{1-x}S$ solid solutions still display higher photocatalytic performance than their CdS and ZnS counterparts. Although the strategy of non-metal doping for enhancing the photocatalytic activity of semiconductors has been widely explored, the correlative research for $Zn_xCd_{1-x}S$ solid solutions is rare. Particularly, P doping can dramatically improve the photocatalytic activity of widely studied photocatalysts, such as TiO_2 and g-C_3N_4 [43]. Considering the advances of P doping and $Zn_xCd_{1-x}S$ solid solutions, it is reasonable to envision that P-doped $Zn_xCd_{1-x}S$ solid solutions ($Zn_xCd_{1-x}S$-P) will exhibit better photocatalytic activities for hydrogen evolution from pure water compared with CdS-P. Herein, we fabricate $Zn_xCd_{1-x}S$-P solid solutions with rich S vacancies and investigate their photocatalytic hydrogen evolution activities from pure water without the assistance of electron sacrificial agents. The strategy of interstitial P doping can effectively elongate the lifetime of charge carriers and enhance the generation and separation of photogenerated electrons-holes, and result in a H_2 evolution rate of $419 \, \mu mol \, h^{-1} \, g^{-1}$, which is 72 and 7.5 times higher than those of ZnS-P ($5.8 \, \mu mol \, h^{-1} \, g^{-1}$) and CdS-P ($56 \, \mu mol \, h^{-1} \, g^{-1}$), respectively. Moreover, the photocatalytic hydrogen evolution reaction can be further promoted when it is coupled with the photocatalytic oxidation of biomass-derived compound 5-hydroxymethylfurfural into 2,5-diformylfuran.

2. Experimental

2.1. Materials

Cadmium acetate dihydrate ($Cd(OAc)_2·2H_2O$, Guangdong Xilong Chemical Company, 99.5%), zinc acetate dihydrate ($Zn(OAc)_2·2H_2O$, Tianjin Jinke Institute of Fine Chemicals, 99.0%), thiourea (Beijing Chemical Reagent Company, 99.0%), hydrazine monohydrate ($H_4N_2·H_2O$, Energy Chemical, 80%), sodium hypophosphite (NaH_2PO_2, Aladdin, 99.0%), and 5-hydroxymethylfurfural (HMF, Aladdin, 95.0%). All chemicals were reagent grade and used as received without further purification.

2.2. Preparation of $Zn_xCd_{1-x}S$

In a typical synthesis of $Zn_{0.5}Cd_{0.5}S$ solid solution, a mixture of 1 mmol $Zn(OAc)_2·2H_2O$, 1 mmol $Cd(OAc)_2·2H_2O$, and 2 mmol thiourea were dissolved in 75 mL deionized water via vigorous stirring for 1 h at room temperature. After adding 5 mL $H_4N_2·H_2O$, the solution was transferred into a 100 mL Teflon-lined stainless autoclave. Afterward, the autoclave was sealed and heated to 180 °C and maintained at the temperature for 24 h, and then cooled down to room temperature in an electric oven. The $Zn_{0.5}Cd_{0.5}S$ solid solution with rich S vacancies was obtained by centrifugation, washed with deionized water thoroughly, and dried in oven at 50 °C overnight. Similarly, other $Zn_xCd_{1-x}S$ ($0 \leq x \leq 1$) solid solutions were produced using the method described above with the variation in the amount of $Zn(OAc)_2·2H_2O$ and Cd $(OAc)_2·2H_2O$.

2.3. Preparation of $Zn_xCd_{1-x}S$-P

To prepare $Zn_xCd_{1-x}S$-P ($0 \leq x \leq 1$) solid solutions, the obtained 100 mg $Zn_xCd_{1-x}S$ and 500 mg NaH_2PO_2 were mechanically grounded down into powder using an agate mortar and pestle. Subsequently, the mixture powder was transferred to a quartz boat, heated to 300 °C at a ramping rate of $2 °C min^{-1}$, kept at the temperature for 120 min, and cooled down to ambient temperature in Ar flow. After that, the obtained powder was washed with deionized water thoroughly. After drying in a vacuum oven, the $Zn_xCd_{1-x}S$-P solid solutions with rich S vacancies were obtained.

2.4. Characterization

The in situ electron paramagnetic resonance (EPR) measurement was carried out using an Endor spectrometer (Bruker E500) at room temperature. Powder X-ray diffraction (XRD) patterns were recorded using a Bruker AXS D8 X-ray diffractometer with Cu Kα ($\lambda = 1.54056$ Å) radiation. The morphology, lattice fringes, energy dispersive X-ray spectroscopy (EDX), and elemental mapping of the samples were conducted using a transmission electron microscope (TEM, JEM 2100 F) with an accelerating voltage of 200 kV. X-ray photoelectron spectroscopy (XPS) spectra were recorded on ThermoScientific ESCALAB 250XI spectroscopy. UV–vis diffuse reflectance spectra (DRS) were recorded on a spectrophotometer (Hitachi U-3010). Raman measurements were obtained using a Renishaw inVia-Reflex spectrometer equipped with a notch filter and a CCD detector. Time-resolved photoluminescence (TRPL) spectra were excited by Coherent F900 flash lamp. The test samples needed to be prepared as suspension and deoxygenated with Ar for 30 min to remove the air.

2.5. Photocatalytic experiments

The photocatalytic hydrogen production experiments were performed in a 15 mL quartz tube sealed with a silicone rubber septum. In a typical photocatalytic experiment, the tube containing an aqueous solution of 1 mg photocatalyst and 5 mL pure water or 2 mg/mL HMF aqueous solution. Then the system was deoxygenated with Ar for 30 min. White LED light sources (30 × 3 W) were used as the irradiation light source. H_2 was measured by a gas chromatograph (GC-14C, Shimadzu, with Ar as a carrier gas), which was equipped with a 5 Å molecular sieve column (3 m × 2 mm) and a thermal-conductivity detector. The number of incident photons was 1.12×10^{17} photons s^{-1}, which was measured using an irradiance meter. The apparent quantum efficiency (AQE) was calculated according to the equation below:

$$AQE(\%) = \frac{\text{Number of reacted electrons}}{\text{Number of incident photons}} \times 100$$

$$\frac{\text{Number of evolved hydrogen molecules} \times 2}{\text{Number of incident photons}} \times 100$$

The content of H_2O_2 produced during the photocatalytic pure water splitting was measured by UV–vis spectrophotometer. Fe^{2+} can be oxidized into Fe^{3+} by H_2O_2 in an acidic environment (pH = 1–2), and Fe^{3+} combines with KSCN to form $[Fe(SCN)]^{2+}$, which has a maximum absorption peak at 475 nm.

The oxidized products of HMF were determined by gas chromatography-mass spectrometry (GC–MS). GC–MS analysis was performed using Agilent GC-7890 MS-5979 equipped with an autosamler-7693 (Santa Clara, Ca). The GC was equipped with a 30 m (250 μm internal diameter, 0.25 μm film thickness) DB-WAX fused silica capillary column (J W Scientific Folsom, CA). The injection port, ion source and interface temperatures were 200 °C, 220 °C, and 240 °C, respectively. The GC temperature program was 70 °C for 2 min, then $10 °C min^{-1}$ to 200 °C and held for 20 min. The MS was operated in selected ion monitoring mode (SIM). The MS was set as follow: m/z 124 for 2,5-diformylfuran (DFF) and m/z 126 for HMF.

2.6. Electrochemical and photoelectrochemical measurements

Electrochemical and photoelectrochemical measurements were conducted using an electrochemical workstation (CHI 660 C, CH Instruments Inc., Shanghai) via a standard three-electrode system. The working electrodes were prepared as follows: 5 mg photocatalyst powder was dispersed in 1 mL water, and then the mixture was ultrasonicated for 3 h. Next, 200 μL the prepared slurry was transferred onto the ITO with 1 cm^2 illuminated area. Finally, the as-prepared photocatalyst film was dried at room temperature. Meanwhile, an Ag/AgCl electrode (saturated KCl), a piece of Pt sheet, and 0.1 M Na_2SO_4 solution were used as reference electrode, counter electrode, and electrolyte solution, respectively. The transient photocurrent responses were measured with the lamp on and off at a fixed time interval of 20 s under a constant applied bias of 0.2 V. Nevertheless, Mott-Schottky plots measurements were performed using platinum wire as counter electrode and saturated calomel electrode (SCE) as reference electrode.

3. Results and discussion

$Zn_xCd_{1-x}S$ ($0 \le x \le 1$) solid solutions were successfully prepared via a facile hydrothermal method with a small quantity of $H_4N_2 \cdot H_2O$ as a reducing agent. The Zn^{2+} and Cd^{2+} of the samples were reduced to a slightly lower valence state by H_2 decomposed from $H_4N_2 \cdot H_2O$ during the hydrothermal process. To keep the charge balance, the total amount of S atoms should decrease leading to the generation of S vacancies [44,45]. The formation of rich S vacancies in $Zn_xCd_{1-x}S$ solid solutions was verified directly by the room-temperature EPR spectroscopy. It can be seen from Fig. S1 that a strong signal located at g = 2.003 is detected in $Zn_{0.5}Cd_{0.5}S$ [46,47]. As shown in Fig. 1a, the diffraction peaks of CdS (x = 0) and ZnS (x = 1) can be assigned to hexagonal CdS (JCPDS: 41-1049) and hexagonal ZnS (JCPDS: 39-1363), respectively. As the value

of x increases, the diffraction peaks of $Zn_xCd_{1-x}S$ shift continuously to higher diffraction angles and the corresponding crystal phases gradually change from the hexagonal of CdS to that of ZnS, indicating that the synthesized samples are not physical mixtures of CdS and ZnS, but homogeneous $Zn_xCd_{1-x}S$ solid solutions [30,31]. Then $Zn_xCd_{1-x}S$-P ($0 \le x \le 1$) solid solutions were prepared via a thermal phosphorization reaction using NaH_2PO_2 as the P source. After phosphorization calcination, the XRD patterns of $Zn_xCd_{1-x}S$-P are almost identical to those of pristine solid solutions (Fig. 1b). However, Fig. 1c shows a careful comparison of XRD patterns of $Zn_{0.5}Cd_{0.5}S$ and $Zn_{0.5}Cd_{0.5}S$-P. It is noticeable that the main three diffraction peaks of $Zn_{0.5}Cd_{0.5}S$ in the range of 24.5-30° slightly shift to smaller diffraction angles after P doping (inset in Fig. 1c), and the similar phenomena were also found in CdS-P and ZnS-P (Fig. S2), implying the appearance of lattice expansion after P doping [15]. Additionally, Raman spectroscopy was also used to study the structural modification of the samples (Fig. 1d). The energy of the excitation light is 532 nm. Obviously, both $Zn_{0.5}Cd_{0.5}S$ and $Zn_{0.5}Cd_{0.5}S$-P have two characteristic peaks. The peak located at about 300 cm^{-1} corresponds to the first-order longitudinal optical (1-LO) mode and the other peak situated at about 600 cm^{-1} corresponds to the 2-LO, which is consistent with previous reports [48]. Moreover, the 1-LO and 2-LO peaks of $Zn_{0.5}Cd_{0.5}S$-P shift to lower wave numbers with respect to those of $Zn_{0.5}Cd_{0.5}S$, which can be attributed to the lattice expansion along the c-axis [49]. The information obtained from XRD and Raman implies that P has been successfully doped into the lattice of $Zn_{0.5}Cd_{0.5}S$ solid solution.

The morphology and micro-structure of the obtained samples were characterized by TEM. The TEM image (Fig. 2a) displays that the morphology of $Zn_{0.5}Cd_{0.5}S$ is inhomogeneous nanoparticle with a diameter in the range of 20–60 nm. Fig. 2b shows the corresponding high-resolution TEM (HRTEM) image in which the distinct lattice fringes with 0.314 nm spacing can be assigned to the (101) plane of
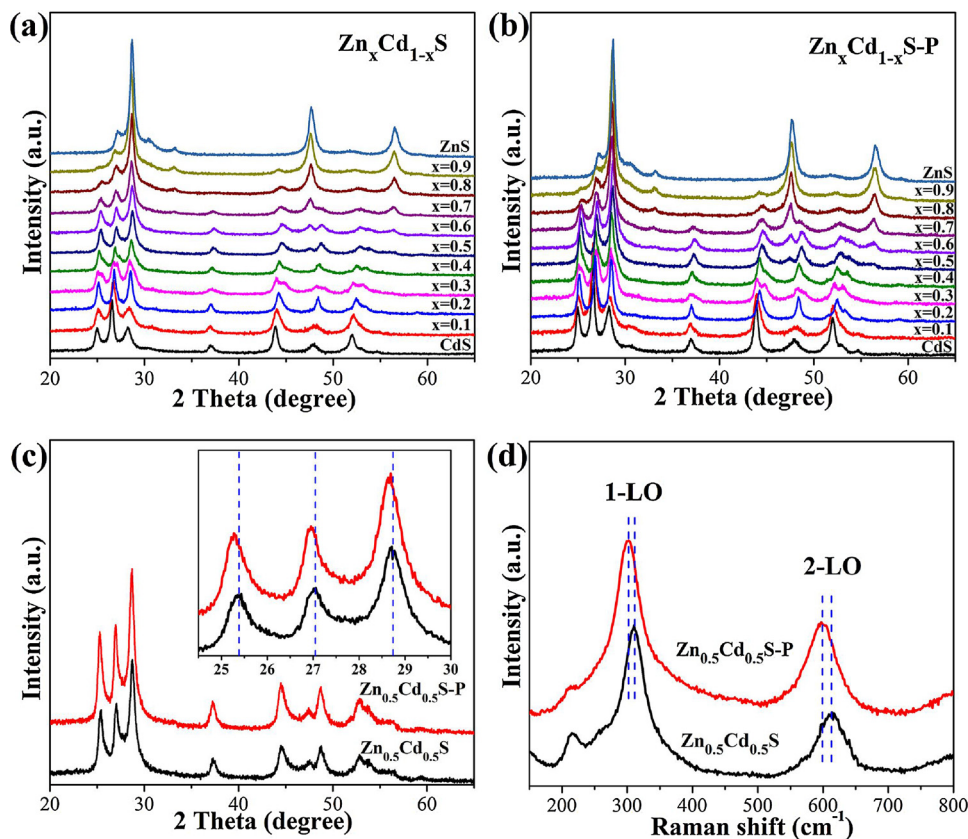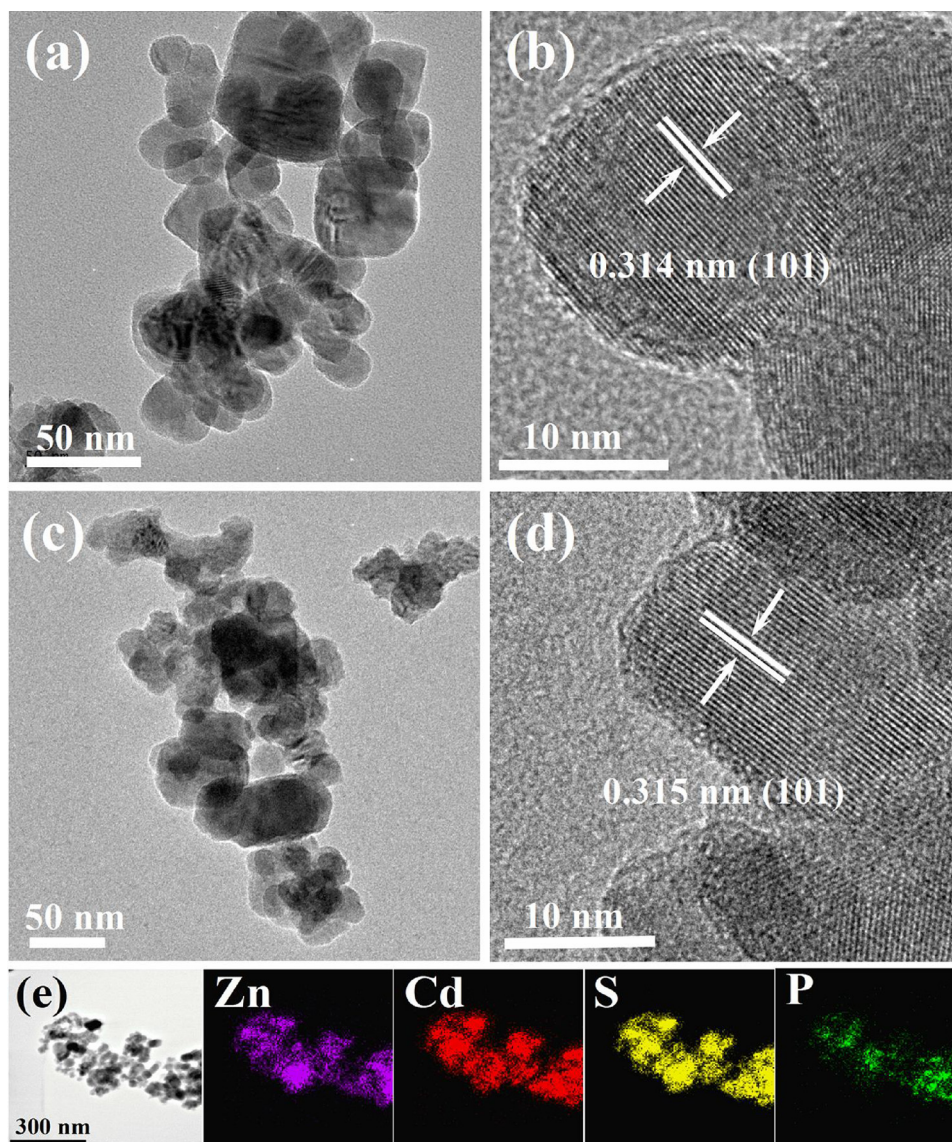

Fig. 1. XRD patterns of (a) $Zn_xCd_{1-x}S$ and (b) $Zn_xCd_{1-x}S$-P ($0 \le x \le 1$) solid solutions. (c) XRD patterns and (d) Raman spectra of $Zn_{0.5}Cd_{0.5}S$ and $Zn_{0.5}Cd_{0.5}S$-P (inset in Fig. 1c: magnified patterns in the range of 24.5–30°).

Fig. 2. (a) TEM and (b) HRTEM images of $Zn_{0.5}Cd_{0.5}S$. (c) TEM and (d) HRTEM images of $Zn_{0.5}Cd_{0.5}S$-P. (e) STEM and elemental mapping images of $Zn_{0.5}Cd_{0.5}S$-P.

$Zn_{0.5}Cd_{0.5}S$. The morphology of $Zn_{0.5}Cd_{0.5}S$-P is almost the same as that of $Zn_{0.5}Cd_{0.5}S$ (Fig. 2c), indicating that the phosphorization process has no obvious effect on the morphology of the solid solution [50,51]. Nevertheless, the lattice fringes spacing of (101) plane of $Zn_{0.5}Cd_{0.5}S$-P is measured as 0.315 nm, which is slightly larger than that of $Zn_{0.5}Cd_{0.5}S$ (Fig. 2d). The expansion of the lattices can be assigned to P doping. The similar phenomena of lattice expansion after P doping were also found in CdS-P (Fig. S3) and ZnS-P (Fig. S4). The scanning TEM (STEM) and corresponding elemental mapping images of $Zn_{0.5}Cd_{0.5}S$-P (Fig. 2e) indicate that Zn, Cd, S, and P elements distribute uniformly in the sample, and the atomic ratio of Zn:Cd:S:P was estimated to be 0.50:0.50:0.95:0.15 matching the result of EDX (Fig. S5). The above results further confirm the successful formation of solid solutions and incorporation of a small amount of P into the samples via phosphorization.

The chemical states of the elements and the doping form of P in the solid solutions were further investigated by XPS. The binding energy scales were calibrated by setting the C 1 s peaks at 284.8 eV as reference (Fig. 3f). The survey spectra (Fig. 3a) indicate the presence of Zn, Cd, and S elements in $Zn_{0.5}Cd_{0.5}S$ and $Zn_{0.5}Cd_{0.5}S$-P, while a small quantity of P is detected in $Zn_{0.5}Cd_{0.5}S$-P. Fig. 3b–e show the high resolution XPS spectra of P 2p, Zn 2p, Cd 3d, and S 2p of the samples. As shown in

Fig. 3b, three peaks approximately at 129.8, 130.6, and 133.7 eV can be assigned to P $2p_{3/2}$, P $2p_{1/2}$, and surface oxidized phosphorus (P–O)-formed during synthesis respectively, indicating that valence state of the P atoms in the solid solution is basically zero valence [52–54]. Furthermore, for both of $Zn_{0.5}Cd_{0.5}S$ and $Zn_{0.5}Cd_{0.5}S$-P, the peaks located at 1022.0 and 1045.0 eV can be assigned to Zn $2p_{3/2}$ and Zn $2p_{1/2}$ (Fig. 3c), while the peaks observed at 405.1 and 411.9 eV belong to Cd $3d_{5/2}$ and Cd $3d_{3/2}$ (Fig. 3d), and the peaks found at 161.7 and 162.8 eV correspond to S $2p_{3/2}$ and S $2p_{1/2}$ (Fig. 3e), respectively [38,55]. Given that the binding energies of Zn and Cd of $Zn_{0.5}Cd_{0.5}S$-P are unchanged relative to those of $Zn_{0.5}Cd_{0.5}S$, it is very unlikely that P atoms can substitute S sites to form Cd-P or Zn-P bonds [43]. Hence, it can be speculated that P atoms are interstitial doped into the framework of $Zn_{0.5}Cd_{0.5}S$. This conclusion was further verified by the concordant XPS results of CdS-P (Fig. S6) and ZnS-P (Fig. S7).

To ascertain the effect of interstitial P doping for the relevant energy levels of the electronic band, UV–vis diffuse reflectance spectra (DRS), XPS valence band spectra, and Mott-Schottky plots of $Zn_{0.5}Cd_{0.5}S$ and $Zn_{0.5}Cd_{0.5}S$-P were determined. The light absorption property of the as-prepared samples studied by UV–vis DRS is displayed in Fig. 4a. The absorption edge of pristine $Zn_{0.5}Cd_{0.5}S$ occurs at about 530 nm. Meanwhile, $Zn_{0.5}Cd_{0.5}S$-P shows a slightly redshift and a strong

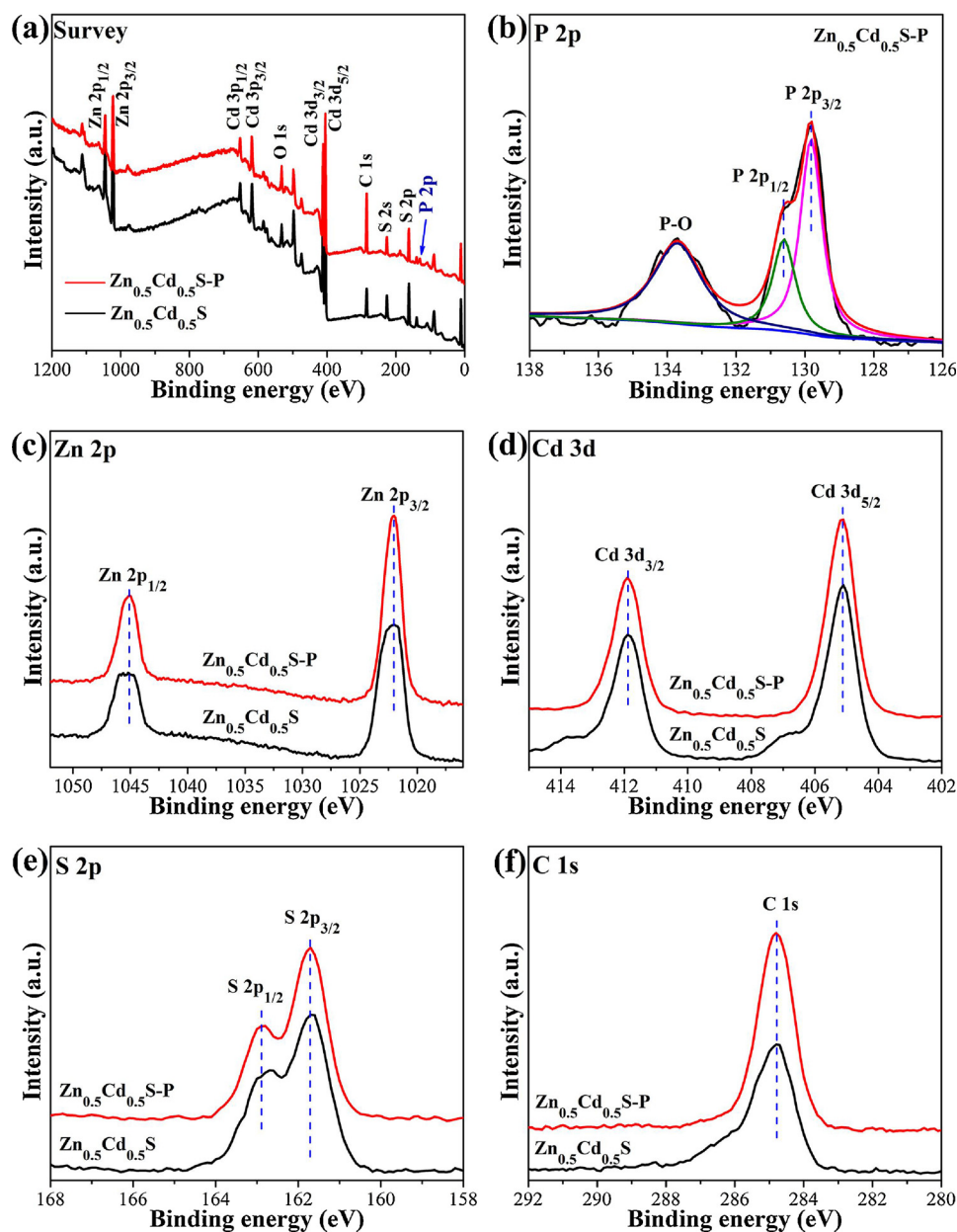**Fig. 3.** (a) XPS survey spectra of $Zn_{0.5}Cd_{0.5}S$ and $Zn_{0.5}Cd_{0.5}S$-P. High resolution XPS spectra of (b) P 2p, (c) Zn 2p, (d) Cd 3d, (e) S 2p, and (f) C 1s of $Zn_{0.5}Cd_{0.5}S$ and $Zn_{0.5}Cd_{0.5}S$-P.

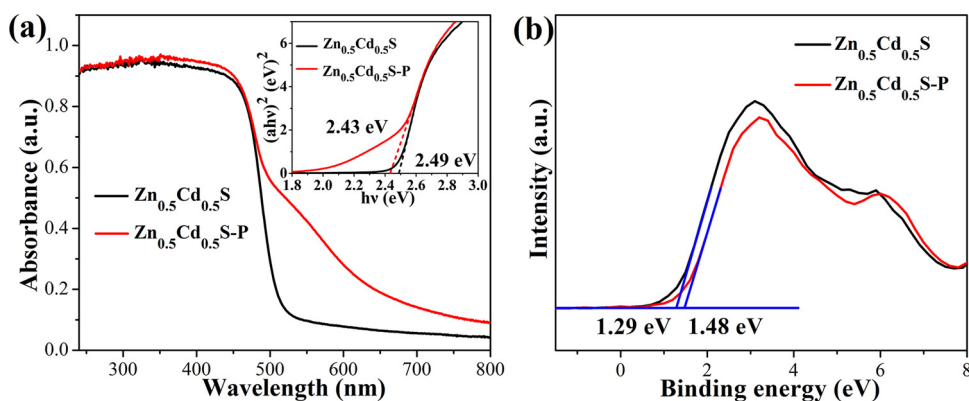**Fig. 4.** (a) UV–vis diffuse reflection spectra and (b) XPS valence band spectra of $Zn_{0.5}Cd_{0.5}S$ and $Zn_{0.5}Cd_{0.5}S$-P (inset in Fig. 4a: band gap energies of the samples).

absorption tail in 500–800 nm, which is due to the introduction of P [15,56]. The UV–vis DRS spectra of CdS-P and ZnS-P are displayed in Fig. S8. Interstitial P doping induces a remarkable enhancement in the optical absorption, which is beneficial to the improvement of photocatalytic activity. In addition, the band gap energies (E_g) of $Zn_{0.5}Cd_{0.5}S$ and $Zn_{0.5}Cd_{0.5}S$-P (inset in Fig. 4a) were determined from a plot of $(ah\nu)^2$ versus energy ($h\nu$) [57,58], and estimated to be 2.49 and 2.43 eV, respectively. According to the literature, the composition of $Zn_{0.5}Cd_{0.5}S$ conduction band (CB) is unchanged after interstitial P doping, then the CB energy level of $Zn_{0.5}Cd_{0.5}S$-P is equal to that of undoped one [15]. Hence, the valence band (VB) position of $Zn_{0.5}Cd_{0.5}S$-P is 0.06 eV higher than that of $Zn_{0.5}Cd_{0.5}S$. The XPS valence band spectra of $Zn_{0.5}Cd_{0.5}S$ and $Zn_{0.5}Cd_{0.5}S$-P are shown in Fig. 4b. The valence band maximum (VBM) read from XPS valence band spectrum is referred to the Fermi level of the material. By carefully analyzing absorption edge of $Zn_{0.5}Cd_{0.5}S$ and $Zn_{0.5}Cd_{0.5}S$-P, we find that the VBM of $Zn_{0.5}Cd_{0.5}S$-P is larger than that of $Zn_{0.5}Cd_{0.5}S$ by 0.19 eV. Given that the VB position level is raised about 0.06 eV after interstitial P doping, it can be concluded that the Fermi level of $Zn_{0.5}Cd_{0.5}S$-P has a promotion about 0.25 eV.

In addition, the promotion of Fermi level of $Zn_{0.5}Cd_{0.5}S$-P after interstitial P doping was further verified by the analysis of flatband potential (V_{fb}) of the samples, which was quantified by the Mott-Schottky (M-S) plots at frequencies 1.5, 2.0, and 2.5 kHz in 0.1 M Na_2SO_4 solution. As shown in Fig. 5, $Zn_{0.5}Cd_{0.5}S$ and $Zn_{0.5}Cd_{0.5}S$-P both show a positive slope in M-S plots regardless of test frequency, which means that they both exhibit *n*-type semiconductor characteristics [59,60]. The V_{fb} of $Zn_{0.5}Cd_{0.5}S$ is determined to be −1.60 eV (Fig. 5a). Compared with $Zn_{0.5}Cd_{0.5}S$, the V_{fb} of $Zn_{0.5}Cd_{0.5}S$-P is upgraded to −1.85 eV (Fig. 5b), proving the formation of a stronger *n*-type semiconductor. Given that the V_{fb} of sample is the difference between Fermi level and water-reduction potential [61], the Fermi level of $Zn_{0.5}Cd_{0.5}S$-P is raised up 0.25 eV compared with that of $Zn_{0.5}Cd_{0.5}S$, which is consistent with results of UV–vis DRS and XPS valence band. On the basis of previous reference, the impurity level of S vacancies is a shallow trap state, and locates between the conduction band and Fermi level [62]. According to the classical theory of semiconductor physics, the impurity level can act as an electron trap center when it is located near the Fermi level, and the Fermi level can be promoted through doping with a donor impurity [15]. Based on the results of UV–vis DRS spectra, XPS valence band spectra, and Mott-Schottky plots, the impurity level of S vacancies in $Zn_{0.5}Cd_{0.5}S$-P is closer to the Fermi level than that in $Zn_{0.5}Cd_{0.5}S$. Hence, it is a reasonable anticipation that the S vacancies will become excellent electron trap centers after P doping.

To clarify the function of S vacancies as effective electrons trap centers after P doping in the solid solutions, time-resolved photoluminescence (TRPL) spectra of $Zn_{0.5}Cd_{0.5}S$ and $Zn_{0.5}Cd_{0.5}S$-P were

Samples	τ_1 (ns)	Rel. (%)	τ_2 (ns)	Rel. (%)	τ (ns)
$Zn_{0.5}Cd_{0.5}S$	0.577	46.079	5.655	53.921	3.31
$Zn_{0.5}Cd_{0.5}S$-P	0.905	29.403	5.954	70.597	4.47
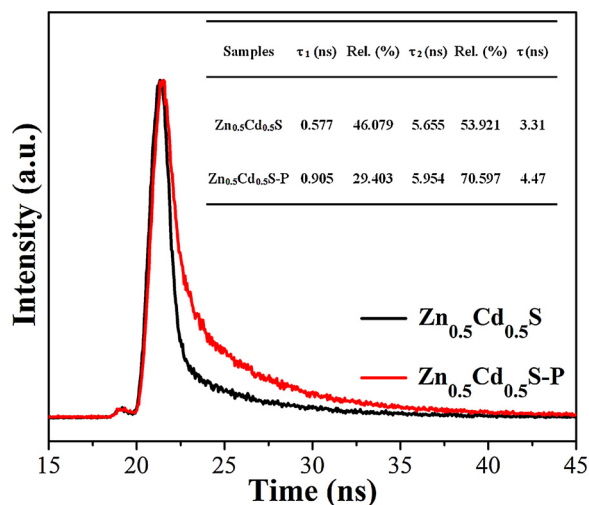
Fig. 6. Time-resolved photoluminescence spectra of $Zn_{0.5}Cd_{0.5}S$ and $Zn_{0.5}Cd_{0.5}S$-P.

investigated. The TRPL spectra (Fig. 6) were conducted to gain the photogenerated charge carriers lifetime in the samples, and the relevant radiative lifetimes and their percentages are inserted in Fig. 6 [63]. Compared with $Zn_{0.5}Cd_{0.5}S$ (∼3.31 ns), $Zn_{0.5}Cd_{0.5}S$-P shows an increased intensity-average PL lifetime (∼4.47 ns), which is attributed to the fact that S vacancies become electron trap centers in $Zn_{0.5}Cd_{0.5}S$-P according to the above UV–vis DRS, XPS valence band and M-S plot results. The long-lived photogenerated electrons represent a higher probability of their involvement in the photocatalytic reaction before recombination.

It is well known that the excitation and transfer of the photogenerated electron-hole pairs of photocatalyst mainly determines its photocatalytic activity [64]. It can be seen from Fig. 7a that the photocurrent of $Zn_{0.5}Cd_{0.5}S$ enhances obviously after interstitial P doping, and the corresponding photocurrent density changes from 0.85 to 2.85 μA/cm^2, indicating a notable promotion of generation and separation of photogenerated electrons-holes. In accordance with the photocurrents, EIS Nyquist plots also show a similar result (Fig. 7b). When angular frequency is at high frequencies, the rate of charge transfer at the electrode interface is the rate control step throughout the electrochemical reaction system. The diameter of the arc radius on the EIS Nyquist plot of $Zn_{0.5}Cd_{0.5}S$-P is much smaller than that of undoped $Zn_{0.5}Cd_{0.5}S$, which suggests a smaller interface resistance for $Zn_{0.5}Cd_{0.5}S$-P [64,65]. Furthermore, an direct comparison of M-S plots at frequency 2.0 kHz is shown in Fig. 7c, the M-S plot of $Zn_{0.5}Cd_{0.5}S$-P shows a smaller slope with respect to that of $Zn_{0.5}Cd_{0.5}S$, meaning that
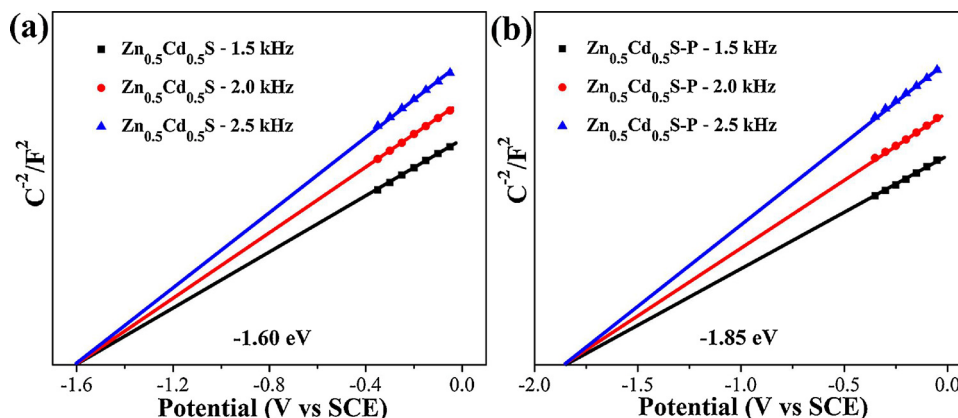
Fig. 5. Mott-Schottky plots of (a) $Zn_{0.5}Cd_{0.5}S$ and (b) $Zn_{0.5}Cd_{0.5}S$-P at frequencies 1.5, 2.0, and 2.5 kHz in 0.1 M Na_2SO_4 solution. (For interpretation of the references to colour in this figure legend, the reader is referred to the web version of this article.)
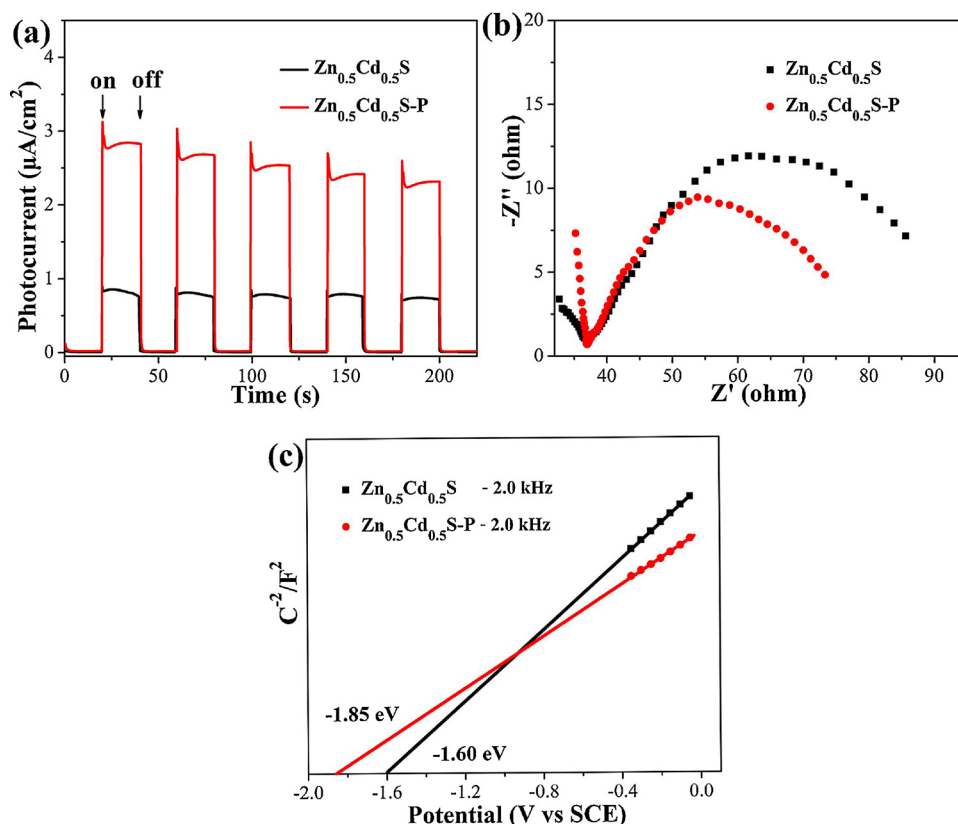
Fig. 7. (a) Transient photocurrent response curves, (b) Electrochemical impedance spectroscopy (EIS) Nyquist plots, and (c) M-S plots of $Zn_{0.5}Cd_{0.5}S$ and $Zn_{0.5}Cd_{0.5}S$-P.

$Zn_{0.5}Cd_{0.5}S$-P possesses a higher carrier concentration [59,60]. In summary, the elongated lifetime of charge carriers and enhanced generation and separation of photogenerated electrons-holes caused by interstitial P doping in the solid solutions are beneficial to the improvement of photocatalytic activity.

The photocatalytic hydrogen evolution from pure water without the assistance of electron sacrificial agents was evaluated by $Zn_xCd_{1-x}S$ and $Zn_xCd_{1-x}S$-P $(0 \leq x \leq 1)$ under visible light irradiation. Fig. 8 displays the comparison of photocatalytic hydrogen evolution rates of the samples. Unfortunately, no H_2 production was detected for all of $Zn_xCd_{1-x}S$ solid solutions in the absence of electron sacrificial reagents
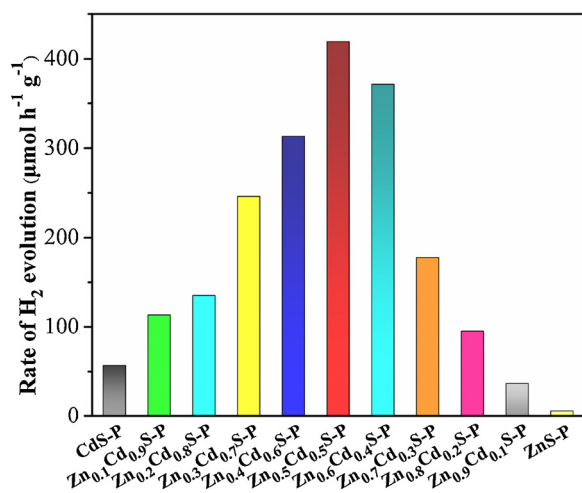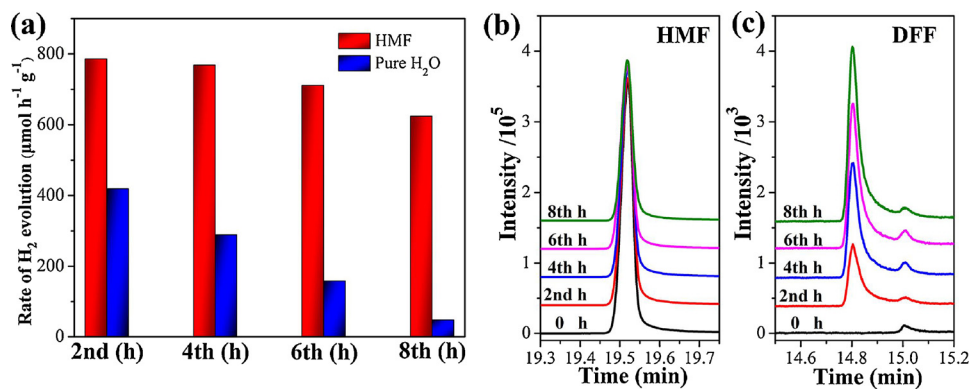

Fig. 8. Comparison of photocatalytic hydrogen evolution rates of $Zn_xCd_{1-x}S$-P $(0 \leq x \leq 1)$ solid solutions from pure water without using of any electron sacrificial agents.

after 2 h irradiation. However, after interstitial P doping, all of $Zn_xCd_{1-x}S$-P solid solutions exhibit relatively high photocatalytic activities under the same conditions. The photocatalytic activity first increases and then decreases with the increment of Zn content in the solid solutions. Notably, $Zn_{0.5}Cd_{0.5}S$-P gives a maximum H_2 evolution rate (419 $\mu mol\,h^{-1}\,g^{-1}$), which is 72 and 7.5 times higher than those of ZnS-P (5.8 $\mu mol\,h^{-1}\,g^{-1}$) and CdS-P (56 $\mu mol\,h^{-1}\,g^{-1}$), respectively. The AQE of $Zn_{0.5}Cd_{0.5}S$-P was calculated to be 0.12%. Therefore, the introduction of interstitial P endows the $Zn_xCd_{1-x}S$ solid solutions visible light photocatalytic activity for H_2 evolution from pure water without using of any electron sacrificial agents. Meanwhile, the effect of P doping concentration was also investigated. The photocatalytic hydrogen evolution rates of $Zn_{0.5}Cd_{0.5}S$-P samples synthesized by varying the mass ratio of $Zn_{0.5}Cd_{0.5}S/NaH_2PO_2$ from pure water are shown in Fig. S9. The photocatalytic activity first increases and then decreases with the increment mass ratio of NaH_2PO_2, the $Zn_{0.5}Cd_{0.5}S$-P sample synthesized using the mass ratio of $Zn_{0.5}Cd_{0.5}S/NaH_2PO_2 = 1:5$ possesses the best photocatalytic activity. Unfortunately, no O_2 was detected in this reaction system, which is likely due to its redox potential [30]. Firstly, the overpotential for O_2 evolution through four electrons pathway is very large; secondly, the valence band position is shifted upward after P doping. Instead, a small amount of H_2O_2 through single electron pathway by photogenerated holes was observed in the $Zn_{0.5}Cd_{0.5}S$-P system (Fig. S10), and the concentration of H_2O_2 gradually increased over 8 h illumination, which can be mainly attributed to the complex thermodynamics of photocatalytic oxygen evolution from water [15]. Considering the low efficiency of overall water splitting, it is highly desirable to replace the water oxidation reaction by a more thermodynamics favorable and valuable HMF oxidation reaction.

In order to improve solar energy conversion efficiency, photocatalytic oxidation of biomass-derived compound HMF was introduced into the photocatalytic system. A comparison of the photocatalytic H_2 evolution rates of $Zn_{0.5}Cd_{0.5}S$-P combined with or without

Fig. 9. (a) Comparison of photocatalytic H_2 evolution rates of $Zn_{0.5}Cd_{0.5}$S-P from pure water and HMF aqueous solution, and (b and c) GC–MS traces of photocatalytic oxidation of HMF by $Zn_{0.5}Cd_{0.5}$S-P.
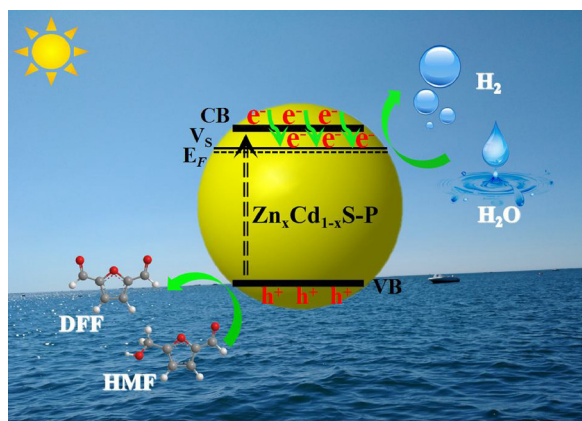
Fig. 10. Schematic illustration of effective photocatalytic hydrogen evolution from water coupled with photocatalytic oxidation of HMF over Zn_xCd_{1-x}S-P under visible light irradiation.

photocatalytic oxidation of HMF is displayed in Fig. 9a. Notably, the photocatalytic activity of $Zn_{0.5}Cd_{0.5}$S-P is significantly enhanced and the H_2 evolution rate increases to $786\ \mu mol\ h^{-1}\ g^{-1}$ in the present of HMF (2 mg/mL). Moreover, $Zn_{0.5}Cd_{0.5}$S-P can maintain good photocatalytic stability when coupled with photocatalytic oxidation of HMF. The H_2 evolution rate of $Zn_{0.5}Cd_{0.5}$S-P is $623\ \mu mol\ h^{-1}\ g^{-1}$ after 8 h of irradiation. The XRD pattern (Fig. S11) and TEM image (Fig. S12) of the used $Zn_{0.5}Cd_{0.5}$S-P are consistent with those of the fresh sample. The slight decrease of photocatalytic activity might be mainly related to the consumption of HMF in the solution. The enhancement of photocatalytic hydrogen evolution and stability of $Zn_{0.5}Cd_{0.5}$S-P can be mainly attributed to effective utilization of photogenerated holes during the progress of HMF oxidation, which can availably promote the separation of photogenerated charges and depress the photocorrosion of the solid solution. In addition, the organic products from HMF oxidation were identified by GC–MS. The peaks located at about 19.5 min can be assigned to HMF (Fig. 9b), while the peaks observed at around 14.8 min belong to 2,5-diformylfuran (DFF) (Fig. 9c). The GC–MS results evidently exhibit a decrease of the peak for HMF and a rise of the peak for DFF over the irradiation time, indicating the conversion from HMF to DFF. After 8 h of irradiation, conversion of HMF is about 40%, and the selectivity of DFF is about 65%. The corresponding conversion of HMF, yield of the oxidation product DFF, and H_2 evolution amount during the photocatalysis is shown in Fig. S13. As the main product of photocatalytic oxidation of HMF, DFF is a very important monomer of furan-based biopolymers as well as versatile chemical intermediate of functional polymers, pharmaceuticals and heterocyclic ligands [24,66–69]. GC–MS traces of oxidation of HMF without photocatalyst under illumination are shown in Fig. S14. The oxidation of HMF is

negligible after 8 h of irradiation, which further illustrates that the DFF is produced by photocatalytic oxidation. Therefore, the enhanced photocatalytic H_2 evolution activity and value-added oxidation product are achieved by adding biomass derivate compound HMF in water over $Zn_{0.5}Cd_{0.5}$S-P under visible light irradiation, and a schematic illustration is proposed as displayed in Fig. 10.

4. Conclusion

In summary, we have successfully synthesized interstitial P-doped Zn_xCd_{1-x}S solid solutions with rich S vacancies as potocatalysts for photocatalytic hydrogen evolution from pure water without using of any electron sacrificial agents under visible light irradiation. The remarkable photocatalytic activity can be attributed to the elongated lifetime of charge carriers and enhanced generation and separation of photogenerated electrons-holes caused by interstitial P doping in the solid solutions. Notably, $Zn_{0.5}Cd_{0.5}$S-P gives a maximum H_2 evolution rate of $419\ \mu mol\ h^{-1}\ g^{-1}$, which is 72 and 7.5 times higher than those of ZnS-P and CdS-P, respectively. Furthermore, when coupling with thermodynamics favorable photocatalytic oxidation reaction of biomass-derived HMF, the H_2 evolution rate of $Zn_{0.5}Cd_{0.5}$S-P further increases to $786\ \mu mol\ h^{-1}\ g^{-1}$. Meanwhile, one of the value-added HMF oxidation products DFF is simultaneously achieved, which is a very important monomer and versatile chemical intermediate in industry. This present study is anticipated to provide a new opportunity to utilize P-doped semiconductor photocatalysts and valuable photocatalytic oxidation reactions in the design of highly efficient photocatalytic water splitting systems.

Appendix A. Supplementary data

Supplementary material related to this article can be found, in the online version, at doi:https://doi.org/10.1016/j.apcatb.2018.03.060.

References

[1] A. Kudo, Y. Miseki, Heterogeneous photocatalyst materials for water splitting, Chem. Soc. Rev. 38 (2009) 253–278.
[2] X.B. Chen, S.H. Shen, L.J. Guo, S.S. Mao, Semiconductor-based photocatalytic hydrogen generation, Chem. Rev. 110 (2010) 6503–6570.
[3] K. Maeda, Z-scheme water splitting using two different semiconductor photocatalysts, ACS Catal. 3 (2013) 1486–1503.
[4] J.R. Ran, J. Zhang, J.G. Yu, M. Jaroniec, S.Z. Qiao, Earth-abundant cocatalysts for

semiconductor-based photocatalytic water splitting, Chem. Soc. Rev. 43 (2014) 7787–7812.

[5] X. Li, J.G. Yu, J.X. Low, Y.P. Fang, J. Xiao, X.B. Chen, Engineering heterogeneous semiconductors for solar water splitting, J. Mater. Chem. A 3 (2015) 2485–2534.

[6] S.S. Chen, T. Takata, K. Domen, Particulate photocatalysts for overall water splitting, Nat. Rev. Mater. 2 (2017) 17050.

[7] D.D. Zheng, X.N. Cao, X.C. Wang, Precise formation of a hollow carbon nitride structure with a Janus surface to promote water splitting by photoredox catalysis, Angew. Chem. Int. Ed. 55 (2016) 11512–11516.

[8] L.C. Mu, Y. Zhao, A.L. Li, S.Y. Wang, Z.L. Wang, J.X. Yang, Y. Wang, T.F. Liu, R.T. Chen, J. Zhu, F.T. Fan, R.G. Li, C. Li, Enhancing charge separation on high symmetry SrTiO₃ exposed with anisotropic facets for photocatalytic water splitting, Energy Environ. Sci. 9 (2016) 2463–2469.

[9] Q. Zhang, Z. Li, S.Y. Wang, R.G. Li, X.W. Zhang, Z.X. Liang, H.X. Han, S.J. Liao, C. Li, Effect of redox cocatalysts location on photocatalytic overall water splitting over cubic NaTaO₃ semiconductor crystals exposed with equivalent facets, ACS Catal. 6 (2016) 2182–2191.

[10] W. Liu, L.L. Cao, W.R. Cheng, Y.J. Cao, X.K. Liu, W. Zhang, X.L. Mou, L.L. Jin, X.S. Zheng, W. Che, Q.H. Liu, T. Yao, S.Q. Wei, Single-site active cobalt-based photocatalyst with a long carrier lifetime for spontaneous overall water splitting, Angew. Chem. Int. Ed. 56 (2017) 9312–9317.

[11] K. Maeda, M. Higashi, D.L. Lu, R. Abe, K. Domen, Efficient nonsacrificial water splitting through two-step photoexcitation by visible light using a modified oxynitride as a hydrogen evolution photocatalyst, J. Am. Chem. Soc. 132 (2010) 5858–5868.

[12] Q. Wang, T. Hisatomi, Q.X. Jia, H. Tokudome, M. Zhong, C.Z. Wang, Z.H. Pan, T. Takata, M. Nakabayashi, N. Shibata, Y.B. Li, I.D. Sharp, A. Kudo, T. Yamada, K. Domen, Scalable water splitting on particulate photocatalyst sheets with a solar-to-hydrogen energy conversion efficiency exceeding 1%, Nat. Mater. 15 (2016) 611–615.

[13] Q. Wang, T. Hisatomi, Y. Suzuki, Z.H. Pan, J. Seo, M. Katayama, T. Minegishi, H. Nishiyama, T. Takata, K. Seki, A. Kudo, T. Yamada, K. Domen, Particulate photocatalyst sheets based on carbon conductor layer for efficient Z-scheme pure-water splitting at ambient pressure, J. Am. Chem. Soc. 139 (2017) 1675–1683.

[14] X.Q. Wu, J. Zhao, L.P. Wang, M.M. Han, M.L. Zhang, H.B. Wang, H. Huang, Y. Liu, Z.H. Kang, Carbon dots as solid-state electron mediator for BiVO₄/CDs/CdS Z-scheme photocatalyst working under visible light, Appl. Catal. B: Environ. 206 (2017) 501–509.

[15] R. Shi, H.F. Ye, F. Liang, Z. Wang, K. Li, Y.X. Weng, Z.S. Lin, W.F. Fu, C.M. Che, Y. Chen, Interstitial P-doped CdS with long-lived photogenerated electrons for photocatalytic water splitting without sacrificial agents, Adv. Mater. 30 (2018) 1705941.

[16] J.W. Tang, J.R. Durrant, D.R. Klug, Mechanism of photocatalytic water splitting in TiO₂. Reaction of water with photoholes, importance of charge carrier dynamics, and evidence for four-hole chemistry, J. Am. Chem. Soc. 130 (2008) 13885–13891.

[17] J.W. Tang, A.J. Cowan, J.R. Durrant, D.R. Klug, Mechanism of O₂ production from water splitting: nature of charge carriers in nitrogen doped nanocrystalline TiO₂ films and factors limiting O₂ production, J. Phys. Chem. C 115 (2011) 3143–3150.

[18] S.J.A. Moniz, S.A. Shevlin, D.J. Martin, Z.X. Guo, J.W. Tang, Visible-light driven heterojunction photocatalysts for water splitting-a critical review, Energy Environ. Sci. 8 (2015) 731–759.

[19] B.M. Hunter, H.B. Gray, A.M. Müller, Earth-abundant heterogeneous water oxidation catalysts, Chem. Rev. 116 (2016) 14120–14136.

[20] B. You, N. Jiang, X. Liu, Y.J. Sun, Simultaneous H₂ generation and biomass upgrading in water by an efficient noble-metal-free bifunctional electrocatalyst, Angew. Chem. Int. Ed. 55 (2016) 9913–9917.

[21] B. You, X. Liu, N. Jiang, Y.J. Sun, A general strategy for decoupled hydrogen production from water splitting by integrating oxidative biomass valorization, J. Am. Chem. Soc. 138 (2016) 13639–13646.

[22] N. Jiang, B. You, R. Boonstra, I.M.T. Rodriguez, Y.J. Sun, Integrating electrocatalytic 5-hydroxymethylfurfural oxidation and hydrogen production via Co-P-derived electrocatalysts, ACS Energy Lett. 1 (2016) 386–390.

[23] B. You, X. Liu, X. Liu, Y.J. Sun, Efficient H₂ evolution coupled with oxidative refining of alcohols via a hierarchically porous nickel bifunctional electrocatalyst, ACS Catal. 7 (2017) 4564–4570.

[24] G.Q. Han, Y.H. Jin, R.A. Burgess, N.E. Dickenson, X.M. Cao, Y.J. Sun, Visible-light-driven valorization of biomass intermediates integrated with H₂ production catalyzed by ultrathin Ni/CdS nanosheets, J. Am. Chem. Soc. 139 (2017) 15584–15587.

[25] S. Cao, Y. Chen, C.J. Wang, P. He, W.F. Fu, Highly efficient photocatalytic hydrogen evolution by nickel phosphide nanoparticles from aqueous solution, Chem. Commun. 50 (2014) 10427–10429.

[26] Y.F. Yu, J. Zhang, X. Wu, W.W. Zhao, B. Zhang, Nanoporous single-crystal-like CdₓZn₁₋ₓS nanosheets fabricated by the cation-exchange reaction of inorganic-organic hybrid ZnS-amine with cadmium ions, Angew. Chem. Int. Ed. 51 (2012) 897–900.

[27] C.J. Xing, Y.J. Zhang, W. Yan, L.J. Guo, Band structure-controlled solid solution of Cd₁₋ₓZnₓS photocatalyst for hydrogen production by water splitting, Int. J. Hydrogen Energy 31 (2006) 2018–2024.

[28] J.C. Wu, J.W. Zheng, C.L. Zacherl, P. Wu, Z.K. Liu, R. Xu, Hybrid functionals study of band bowing, band edges and electronic structures of Cd₁₋ₓZnₓS solid solution, J. Phys. Chem. C 115 (2011) 19741–19748.

[29] M.C. Liu, D.W. Jing, Z.H. Zhou, L.J. Guo, Twin-induced one-dimensional homojunctions yield high quantum efficiency for solar hydrogen generation, Nat. Commun. 4 (2013) 2278.

[30] Q. Li, H. Meng, P. Zhou, Y.Q. Zheng, J. Wang, J.G. Yu, J.R. Gong, Zn₁₋ₓCdₓS solid solutions with controlled bandgap and enhanced visible-light photocatalytic H₂-production activity, ACS Catal. 3 (2013) 882–889.

[31] Z.W. Mei, M.J. Zhang, J.L. Schneider, W. Wang, N. Zhang, Y.T. Su, B.K. Chen, S.F. Wang, A.L. Rogach, F. Pan, Hexagonal Zn₁₋ₓCdₓS (0.2 ≤ x ≤1) solid solution photocatalysts for H₂ generation from water, Catal. Sci. Technol. 7 (2017) 982–987.

[32] M. Kaur, C.M. Nagaraja, Template-free synthesis of Zn₁₋ₓCdₓS nanocrystals with tunable band structure for efficient water splitting and reduction of nitroaromatics in water, ACS Sustain. Chem. Eng. 5 (2017) 4293–4303.

[33] H.Y. Zhou, Q.Y. Liu, W.M. Liu, J.C. Ge, M.H. Lan, C. Wang, J.X. Geng, P.F. Wang, Template-free preparation of volvox-like CdₓZn₁₋ₓS nanospheres with cubic phase for efficient photocatalytic hydrogen production, Chem. Asian J. 9 (2014) 811–818.

[34] Y. Jin, H.Y. Zhang, C. Song, L.F. Wang, Q.Y. Lu, F. Gao, Hollow ZnₓCd₁₋ₓS nanospheres with enhanced photocatalytic activity under visible light, Sci. Rep. 6 (2016) 29997.

[35] Y.Y. Lee, J.H. Moon, Y.S. Choi, G.O. Park, M.S. Jin, L.Y. Jin, D.H. Li, J.Y. Lee, S.U. Son, J.M. Kim, Visible-light driven photocatalytic degradation of organic dyes over ordered mesoporous CdₓZn₁₋ₓS materials, J. Phys. Chem. C 121 (2017) 5137–5144.

[36] J.M. Chen, J.Y. Chen, Y.W. Li, Hollow ZnCdS dodecahedral cages for highly efficient visible-light-driven hydrogen generation, J. Mater. Chem. A 5 (2017) 24116–24125.

[37] Y.G. Chen, S. Zhao, X. Wang, Q. Peng, R. Lin, Y. Wang, R.G. Shen, X. Cao, L.B. Zhang, G. Zhou, J. Li, A.D. Xia, Y.D. Li, Synergetic integration of Cu₁.₉₄S-ZnₓCd₁₋ₓS heteronanorods for enhanced visible-light-driven photocatalytic hydrogen production, J. Am. Chem. Soc. 138 (2016) 4286–4289.

[38] S.J. Zhao, J.J. Huang, Q.Y. Huo, X.Z. Zhou, W.X. Tu, A non-noble metal MoS₂-Cd0.5Zn0.5S photocatalyst with efficient activity for high H₂ evolution under visible light irradiation, J. Mater. Chem. A 4 (2016) 193–199.

[39] A. Litke, T. Weber, J.P. Hofmann, E.J.M. Hensen, Bottlenecks limiting efficiency of photocatalytic water reduction by mixed Cd-Zn sulfides/Pt-TiO₂ composites, Appl. Catal. B: Environ. 198 (2016) 16–24.

[40] J. Wang, B. Li, J.Z. Chen, N. Li, J.F. Zheng, J.H. Zhao, Z.P. Zhu, Enhanced photocatalytic H₂-production activity of CdₓZn₁₋ₓS nanocrystals by surface loading MS (M = Ni, Co, Cu) species, Appl. Surf. Sci. 259 (2012) 118–123.

[41] A.P. Gaikwad, D. Tyagi, C.A. Betty, R. Sasikala, Photocatalytic and photo electrochemical properties of cadmium zinc sulfide solid solution in the presence of Pt and RuS₂ dual co-catalysts, Appl. Catal. A: Gen. 517 (2016) 91–99.

[42] W. Zhang, Z.Y. Zhong, Y.S. Wang, R. Xu, Doped solid solution: (Zn0.95Cu0.05)₁₋ₓCdₓS nanocrystals with high activity for H₂ evolution from aqueous solutions under visible light, J. Phys. Chem. C 112 (2008) 17635–17642.

[43] Z.F. Hu, Z.R. Shen, J.C. Yu, Phosphorus containing materials for photocatalytic hydrogen evolution, Green Chem. 19 (2017) 588–613.

[44] X.Y. Zhang, Z. Zhao, W.W. Zhang, G.Q. Zhang, D. Qu, X. Miao, S.R. Sun, Z.C. Sun, Surface defects enhanced visible light photocatalytic H₂ production for Zn-Cd-S solid solution, Small 12 (2016) 793–801.

[45] G. Wang, B.B. Huang, Z.J. Li, Z.Z. Lou, Z.Y. Wang, Y. Dai, M.H. Whangbo, Synthesis and characterization of ZnS with controlled amount of S vacancies for photocatalytic H₂ production under visible light, Sci. Rep. 5 (2015) 8544.

[46] C. Xiao, K. Li, J.J. Zhang, W. Tong, Y.W. Liu, Z. Li, P.C. Huang, B.C. Pan, H.B. Su, Y. Xie, Magnetic ions in wide band gap semiconductor nanocrystals for optimized thermoelectric properties, Mater. Horiz. 1 (2014) 81–86.

[47] J.G. Wang, Y.J. Chen, W. Zhou, G.H. Tian, Y.T. Xiao, H.Y. Fu, H.G. Fu, Cubic quantum dot/hexagonal microsphere ZnIn₂S₄ heterophase junctions for exceptional visible-light-driven photocatalytic H₂ evolution, J. Mater. Chem. A 5 (2017) 8451–8460.

[48] Y.C. Zhang, W.W. Chen, X.Y. Hu, Controllable synthesis and optical properties of Zn-doped CdS nanorods from single-source molecular precursors, Cryst. Growth Des. 7 (2007) 580–586.

[49] C. Hu, X.H. Zeng, J.Y. Cui, H.T. Chen, J.F. Lu, Size effects of Raman and photoluminescence spectra of CdS nanobelts, J. Phys. Chem. C 117 (2013) 20998–21005.

[50] C.B. Ouyang, X. Wang, S.Y. Wang, Phosphorus-doped CoS₂ nanosheet arrays as ultra-efficient electrocatalysts for the hydrogen evolution reaction, Chem. Commun. 51 (2015) 14160–14163.

[51] W. Liu, E.Y. Hu, H. Jiang, Y.J. Xiang, Z. Weng, M. Li, Q. Fan, X.Q. Yu, E.I. Altman, H.L. Wang, A highly active and stable hydrogen evolution catalyst based on pyrite-structured cobalt phosphosulfide, Nat. Commun. 7 (2016) 10771.

[52] Z.B. Sun, H.H. Xie, S.Y. Tang, X.F. Yu, Z.N. Guo, J.D. Shao, H. Zhang, H. Huang, H.Y. Wang, P.K. Chu, Ultrasmall black phosphorus quantum dots: synthesis and use as photothermal agents, Angew. Chem. Int. Ed. 54 (2015) 11526–11530.

[53] M.S. Zhu, X.Y. Cai, M. Fujitsuka, J.Y. Zhang, T. Majima, Au/La₂Ti₂O₇ nanostructures sensitized with black phosphorus for plasmon-enhanced photocatalytic hydrogen production in visible and near-infrared light, Angew. Chem. 129 (2017) 2096–2100.

[54] M.S. Zhu, S. Kim, L. Mao, M. Fujitsuka, J.Y. Zhang, X.C. Wang, T. Majima, Metal-free photocatalyst for H₂ evolution in visible to near-infrared region: black phosphorus/graphitic carbon nitride, J. Am. Chem. Soc. 139 (2017) 13234–13242.

[55] M.C. Liu, Y.B. Chen, J.Z. Su, J.W. Shi, X.X. Wang, L.J. Guo, Photocatalytic hydrogen production using twinned nanocrystals and an unanchored NiSₓ co-catalyst, Nat. Energy 1 (2016) 16151.

[56] S.Z. Hu, L. Ma, J.G. You, F.Y. Li, Z.P. Fan, F. Wang, D. Liu, J.Z. Gui, A simple and efficient method to prepare a phosphorus modified g-C₃N4 visible light photocatalyst, RSC Adv. 4 (2014) 21657–21663.

[57] J.G. Song, H.T. Zhao, R.R. Sun, X.Y. Li, D.J. Sun, An efficient hydrogen evolution catalyst composed of palladium phosphorous sulphide (PdP₋₀.₃₃S₋₁.₆₇) and twin nanocrystal Zn0.5Cd0.5S solid solution with both homo- and hetero-junctions, Energy Environ. Sci. 10 (2017) 225–235.

[58] Y. Su, Z. Zhang, H. Liu, Y. Wang, Cd0.2Zn0.8S@UiO-66-NH₂ nanocomposites as

efficient and stable visible-light-driven photocatalyst for H_2 evolution and CO_2 reduction, Appl. Catal. B: Environ. 200 (2017) 448–457.

[59] A.G. Tamirat, W.N. Su, A.A. Dubale, H.M. Chen, B.J. Hwang, Photoelectrochemical water splitting at low applied potential using a NiOOH coated codoped (Sn, Zr) a-Fe2O3 photoanode, J. Mater. Chem. A 3 (2015) 5949–5961.

[60] J.J. Deng, X.X. Lv, J.Y. Liu, H. Zhang, K.Q. Nie, C.H. Hong, J.O. Wang, X.H. Sun, J. Zhong, S.T. Lee, Thin-layer Fe_2TiO_5 on hematite for efficient solar water oxidation, ACS Nano 9 (2015) 5348–5356.

[61] H.M. Huang, B.Y. Dai, W. Wang, C.H. Lu, J.H. Kou, Y. Ni, L.Z. Wang, Z.Z. Xu, Oriented built-in electric field introduced by surface gradient diffusion doping for enhanced photocatalytic H_2 evolution in CdS nanorods, Nano Lett. 17 (2017) 3803–3808.

[62] X.L. Xu, Y.Y. Zhao, E.J. Sie, Y.H. Lu, B. Liu, S.A. Ekahana, X. Ju, Q.K. Jiang, J.B. Wang, H.D. Sun, T.C. Sum, C.H.A. Huan, Y.P. Feng, Q.H. Xiong, Dynamics of bound exciton complexes in CdS nanobelts, ACS Nano 5 (2011) 3660–3669.

[63] J.R. Ran, T.Y. Ma, G.P. Gao, X.W. Du, S.Z. Qiao, Porous P-doped graphitic carbon nitride nanosheets for synergistically enhanced visible-light photocatalytic H_2 production, Energy Environ. Sci. 8 (2015) 3708–3717.

[64] W.J. Jiang, Y.F. Liu, J. Wang, M. Zhang, W.J. Luo, Y.F. Zhu, Separation-free

polyaniline/TiO_2 3D hydrogel with high photocatalytic activity, Adv. Mater. Interfaces 3 (2015) 1500502.

[65] J. Zhang, J.G. Yu, M. Jaroniec, J.R. Gong, Noble metal-free reduced graphene oxide-$Zn_xCd_{1-x}S$ nanocomposite with enhanced solar photocatalytic H_2-production performance, Nano Lett. 12 (2012) 4584–4589.

[66] J.P. Ma, Z.T. Du, J. Xu, Q.H. Chu, Y. Pang, Efficient aerobic oxidation of 5-hydroxymethylfurfural to 2,5-diformylfuran, and synthesis of a fluorescent material, ChemSusChem 4 (2011) 51–54.

[67] S. Yurdakal, B.S. Tek, O. Alagöz, V. Augugliaro, V. Loddo, G. Palmisano, L. Palmisano, Photocatalytic selective oxidation of 5-(hydroxymethyl)-2-furaldehyde to 2,5-furandicarbaldehyde in water by using anatase, rutile, and brookite TiO_2 nanoparticles, ACS Sustain. Chem. Eng. 1 (2013) 456–461.

[68] G.Q. Lv, H.L. Wang, Y.X. Yang, T.S. Deng, C.M. Chen, Y.L. Zhu, X.L. Hou, Graphene oxide: a convenient metal-free carbocatalyst for facilitating aerobic oxidation of 5-hydroxymethylfurfural into 2,5-diformylfuran, ACS Catal. 5 (2015) 5636–5646.

[69] H.L. Zhang, Q. Wu, C. Guo, Y. Wu, T.H. Wu, Photocatalytic selective oxidation of 5-hydroxymethylfurfural to 2,5-diformylfuran over Nb_2O_5 under visible light, ACS Sustain. Chem. Eng. 5 (2017) 3517–3523.